

Slip velocity of large low-aspect-ratio cylinders in homogeneous isotropic turbulence

Margaret L. Byron^{a,b,*}, Yiheng Tao^{a,c}, Isabel A. Houghton^{a,d}, Evan A. Variano^a

^a Civil and Environmental Engineering, University of California Berkeley, Berkeley, CA 94720, USA

^b Mechanical Engineering, Penn State University, State College, PA 16802, USA

^c Civil and Environmental Engineering, Princeton University, Princeton, NJ 08544, USA

^d The Data Institute, University of San Francisco, San Francisco, CA 94105, USA

ARTICLE INFO

Article history:

Received 23 May 2019

Revised 24 August 2019

Accepted 23 September 2019

Available online 26 September 2019

Keywords:

Turbulence

Multiphase

Particle-laden flow

Non-spherical particles

Slip velocity

Settling

ABSTRACT

Using laboratory experiments, we investigate the turbulent slip velocity of large (Taylor-scale), slightly negatively buoyant cylinders at two mass densities and four aspect ratios. Using refractive index matching and stereoscopic Particle Image Velocimetry, we simultaneously record the velocities of both the cylinders and the surrounding homogeneous isotropic turbulence. We find that despite the large size and concomitant inertia of the cylinders, the cylinder velocity is well predicted by the fluid velocity immediately surrounding it: the particle velocity is close to the fluid velocity across a large range of fluid velocities, barring a small slip velocity. We apply a decomposition to this slip velocity and find that its average is nonzero in the vertical direction, indicating gravitational settling, but is approximately zero in the two lateral directions, reflective of the isotropy in the turbulence. The average slip velocity is subtracted from instantaneous slip velocity to find the “true slip”, with the anisotropic effects of gravitational settling ostensibly removed. However, this true slip also shows the effects of gravity, indicating that large particles with even a small departure from neutral buoyancy may sample the flow anisotropically. In other words, gravity creates anisotropy in the slip velocity even without considering the effects of settling/sedimentation. We discuss potential mechanisms for this effect, including preferential concentration and resuspension, and conclude that gravity should be considered in studies of large particles even when the particles are very close to neutrally buoyant.

© 2019 Elsevier Ltd. All rights reserved.

1. Introduction

Interactions between particulate matter and turbulent fluid flow are ubiquitous in the natural and built environment. The motion of individual particles in turbulence is relevant to many scientific and engineering applications, and can help elucidate the mechanics of processes vital to environmental science (e.g., marine aggregation (Kjørboe et al., 1990) or aerosol settling (Maxey, 1987)), industry (e.g., combustion (Yin et al., 2003) or paper fabrication (Lundell et al., 2011)), and civil infrastructure (e.g., sediment transport (Schmeeckle et al., 2001) or water treatment (Bridgeman et al., 2009)). In these cases and others, the relevant particles are frequently larger than the Kolmogorov microscale and often nonspherical, which makes their motion difficult to predict analytically.

Of special interest to us are particles whose sizes are comparable to the Taylor microscale. Such particles are situated within the inertial subrange characteristic of turbulence (Pope, 2001). Therefore, ambient vortex structures will be present at both larger and smaller scales than the particles themselves. This is a unique dynamical regime, particularly when considering the mechanisms by which particles inherit linear and angular momentum from the surrounding turbulence. The effect of such multi-scale forcing on an object's dynamics is an interesting and open question. Particles in this size range are inertial even if they are neutrally buoyant; finite size effects alone will prevent such particles from acting as perfect tracers. In this regime, particle trajectories will deviate (in some cases significantly) from fluid pathlines. This contributes to the establishment of a nontrivial “slip velocity”: the instantaneous difference between the particle's velocity and the local fluid velocity.

* Corresponding author.

E-mail address: mbyron@psu.edu (M.L. Byron).

1.1. Slip velocity definition

The slip velocity of a suspended particle is defined as follows:

$$\mathbf{u}_s \equiv \mathbf{u}_p - \mathbf{u}_f \quad (1)$$

where \mathbf{u}_p is the instantaneous particle center-of-mass velocity, and \mathbf{u}_f is a velocity which is representative of the local instantaneous fluid velocity field. Obtaining the particle velocity is relatively straightforward in both laboratory and numerical experiments. However, there are several choices for the fluid velocity \mathbf{u}_f , the fluid velocity “seen” by the particle. In a numerical experiment, one may obtain \mathbf{u}_f by re-running the simulation with identical initial and boundary conditions, but without particles (Bagchi and Balachandar, 2003a), or (for one-way coupled simulations) use the predetermined fluid velocity at the particle center of mass (Calzavarini et al., 2012). Neither approach is feasible for a laboratory experiment. If the particles are smaller than the scale at which turbulent velocity gradients become linear (the Kolmogorov scale), it is possible to interpolate a velocity to the particle center. However, for large particles, interpolation will not yield a correct estimation of \mathbf{u}_f , nor will that estimation be relevant, since the particle is influenced by more than the point velocity at its center of mass. There is neither a perfect nor universal definition of \mathbf{u}_f in experimental flows, especially for large particles, and so approximations must be made (Bellani and Variano, 2012). In this work, we define an approximate slip velocity from planar laboratory measurements (see Section 2.4).

1.2. Physical significance of the slip velocity

Slip is a key parameter in studies of turbulence modulation via particle loading (Kulick et al., 1994; Ferrante and Elghobashi, 2003). Cisse et al. (2013) studied flow modification due to the slipping between large spherical particles and the surrounding homogeneous turbulence, including the viscous boundary layer around the particle. Zhao et al. (2014) also studied slip velocity in the context of turbulence modulation, investigating the effects of aspect ratio on the slip of long fibers in turbulent channel flow. A very detailed simulation was performed by Zhao and Wachem (2013), in which experimenters used a full four-way coupling scheme. They simulated a turbulent channel flow that is sparsely laden with spherical and ellipsoidal particles, finding not only turbulence modulation but an anisotropic slip velocity (higher in the stream-wise direction). This underscores the importance of the slip velocity in determining the dynamics of both the particles and the surrounding flow. The slip velocity is also the parameter that is most often used to define a particle Reynolds number, which helps categorize wake dynamics (Bagchi and Balachandar, 2002b; 2002a; 2003b).

The slip velocity is closely related to the turbulent settling velocity for a given particle or class of particles, and is of particular use in the context of laboratory experiments. The most straightforward method for calculating an object or particle's settling velocity (measuring the time it takes for the object to fall through a large distance and dividing distance by time) is not always practical or relevant in laboratory turbulent flows. A short observation may not give an accurate measurement, since the vertical velocities of both the particle and the fluid fluctuate strongly. A long observation may not be possible due to experimental constraints. In a bounded tank or vessel, particles may be resuspended after reaching the bottom boundary, so a long time-average of an individual particle's vertical velocity will skew to zero. At steady state, the average vertical velocity of many short-term observations will also converge to zero. The average vertical velocity is therefore less representative of particle settling than the average vertical

slip velocity. Additionally, it is this velocity, and not the absolute particle velocity, that determines the fluid drag on that particle. The average instantaneous slip velocity, therefore, may be used as a proxy for the overall (bulk) particle settling velocity in most cases.

1.3. Turbulent alteration of settling velocity

It is known that turbulence alters the settling velocity of solid particles. However, the mechanisms by which this is accomplished are not yet systematically described, and the topic remains an area of active research. While the effects of shape on quiescent settling velocity are well-explored, shape is less well-studied in turbulence compared to particle size and density. However, it is difficult to use results from quiescent settling to predict the settling behavior of the same particles in turbulence. Below, we discuss the state of the field in three areas: the quiescent settling of nonspherical particles, the turbulent settling of spherical particles, and the turbulent settling of nonspherical particles.

1.3.1. Quiescent settling of nonspherical particles

Motivated by powder settling in chemical processes, Christiansen and Barker (1965) experimentally determined the drag coefficients of cylinders, prisms, disks, and spheres at high Reynolds numbers ($1,000 < Re_p < 300,000$); however, low-to-intermediate Reynolds numbers are more commonly found in such applications. A very useful compendium of drag coefficients in this range for a variety of shapes was compiled by Loth (2008), who reviewed a number of mathematical models to integrate the Stokes and Newton drag regimes. Hölzer and Sommerfeld (2008) provided a somewhat simpler drag model for particles in the same dynamic range which depends only on particle sphericity and particle Re . More recently, advances in experimental methods have enabled precise quantification of particle shape, which—when coupled with advanced imaging techniques—enable a precise analysis of the effects of both shape and orientation on settling velocity (Bagheri and Bonadonna, 2016). Advances in numerical computation have opened detailed views into even small departures from sphericity (Ardekani et al., 2016). Further studies have focused on non-axisymmetric bodies (Esteban et al., 2018; 2019), which display interesting wakes and falling trajectories. However, the effects of shape are more easily quantified in the absence of turbulence, which is often relevant to the original motivating problems.

1.3.2. Turbulent settling of spherical particles

Spherical particles offer many advantages: they are easier to fabricate, can be easier to simulate, and their use enables a broad sweep through a range of size, density, or both, facilitating dimensional analyses which inform our knowledge of the underlying physics (shape, since it is harder to parametrize, lends itself less well to this type of analysis). A large portion of the foundational work in this area was conducted in parallel by two disparate groups: the sediment transport community and the aerosol community. In sediment transport, Murray (1970) studied particle settling at intermediate Reynolds numbers ($20 < Re_p < 80$), and observed a settling velocity in turbulence that was reduced by up to 30% relative to the same particles settling in still water. He attributed this decrease, as did his predecessors, to nonlinearity in the drag force (Field, 1968; Brush et al., 1962). Tooby et al. (1977) demonstrated that large, heavy particles tended to form long-lived circular orbits in regions of the flow which opposed their motion (“vortex-trapping”), effectively decreasing their settling velocity. Both mechanisms (drag non-linearity and vortex trapping) served to reduce the turbulent settling velocity relative to the quiescent settling velocity.

In parallel, many researchers motivated by aerosol-related applications concluded that turbulence *increases* particle settling velocity (Yudine, 1959; Csanady, 1963; Meek and Jones, 1973). A physical mechanism was provided by Maxey (1987), who numerically determined that for inertial particles in a Gaussian random flow, settling velocity was actually enhanced relative to the quiescent settling velocity due to trajectory-biasing effects (Maxey and Corrsin, 1986; Maxey, 1990). The discrepancy between the two communities was reconciled in part by Wang and Maxey (1993), who noted that for larger particles, nonlinear drag effects tempered the settling velocity enhancement.

More recently, Fornari et al. (2016a) found reduced settling in finite-size spheres; they explored different particle specific gravities and established scaling laws for particle displacement (Fornari et al., 2016b). It is therefore clear that several settlement-enhancing and -reducing mechanisms may interact depending on a particle's position in the size/density parameter space, underscoring the importance of considering relative scales: the same particle in two different turbulent flows may behave quite differently.

Above, we have outlined three major mechanisms driving settling-velocity alteration for spheres in turbulence: vortex-trapping (large particles; reduces settling velocity), fast-tracking (small particles; enhances settling velocity), and nonlinear drag (large particles; reduces settling velocity). However, we do not have a firm grasp on when each of these mechanisms come into play, nor how they interact. There may also be other altered-settling mechanisms which have not yet been described. For a collection of experiments and review on this topic, the reader is directed to the work of Nielsen (2007) and Good et al. (2014).

1.3.3. Turbulent settling of nonspherical particles

The turbulent settling of nonspherical particles is important for many engineering and industrial applications. It is especially crucial in environmental turbulence, since natural and biological particles are highly non-spherical (Dietrich, 1982; Mandø and Rosendahl, 2010). However, the study of turbulent settling in non-spheres is subject to both practical and philosophical constraints. Experimentally, it may be difficult or expensive to repeatably fabricate or quantify highly irregular shapes. Numerically, the equations of motion and/or drag coefficients are difficult to incorporate in turbulence, and for particles larger than the smallest flow scales, irregular particle geometries are computationally intensive to mesh and couple. Philosophically, there is no general consensus on how to quantify irregular shapes: any simplification necessarily involves a loss of key information, making it difficult to directly compare studies. Nevertheless, recent work on this topic is encouraging.

A general review of the motion of nonspherical particles in turbulence was conducted by Voth and Soldati (2017). Most studies which specifically examine particle settling focus on sub-Kolmogorov scale particles, where the equation of motion takes as input the (unaltered) flow variables at the location of the particle (Shin and Maxey, 1997; Zhang et al., 2001; Marchioli et al., 2010). For finite-size nonspherical particles (*i.e.* those for which one-way coupling cannot be assumed), computation becomes much more difficult and fully-resolved simulations are rare, particularly those which provide statistical observations rather than the behavior of a single sedimenting particle. Existing larger-scale studies of finite-size nonspheres focus primarily on particle orientation and rotation rather than sedimentation (Do-Quang et al., 2014). At this time, laboratory experiments (such as the recent work by Lopez and Guazzelli (2017) on the settling of inertial fibers through counter-rotating vortices) are a necessary complement to numerics in this area. It is this approach that we here pursue.

In this work, we will use the slip velocity as a proxy to examine the settling behavior of large non-spherical particles. Our experiments are set in the regime where the particle settling veloc-

ity v_q is comparable to the turbulent rms velocity $u_{\tau-}$ that is, the timescale of settling is comparable to the intermediate timescales of the flow (larger than the Kolmogorov timescale and smaller than the integral timescale). Furthermore, we measure particles whose lengthscale is comparable to the Taylor microscale, which is larger than the Kolmogorov microscale but smaller than the integral length scale. We have therefore targeted a point in the parameter space which is intermediate in both length and time scales: a point where we expect interesting interactions to occur.

2. Methods

We measure the kinematics of cylindrical particles of varying aspect ratio, comparing cylinder kinematics across several aspect ratios and two mass densities close to neutral buoyancy. We simultaneously measure the flowfield around each cylinder and examine the effect of instantaneous fluid properties on the cylinders' motion.

Experiments are performed by suspending large refractive-index-matched hydrogel cylinders in a 600-gallon (2.3 m³) stirred-tank facility. This tank is capable of generating an approximately 30 cm × 30 cm × 15 cm volume of homogeneous isotropic turbulence via two facing jet arrays (Fig. 1). Glass tracer microspheres within both the cylinders and the surrounding fluid are imaged via stereoscopic Particle Image Velocimetry (sPIV). This provides measurements of three velocity components in a two-dimensional measurement plane (2D3C velocimetry). In this section, we will describe: 1) The configuration of the tank, along with its measured turbulent statistics; 2) the use of the refractive-index-matched hydrogel particle method; 3) the specifications of the sPIV system, and 4) the analytical approach used to extract cylinders' slip velocity.

2.1. Turbulence tank

Active-grid and other random or semi-random actuation approaches have been frequently employed to generate homogeneous and isotropic (HI) turbulence, from early use in wind tunnels (Makita and Sassa, 1991) to various "turbulence box" approaches, in which the forcing elements are symmetrically arranged about a central volume (Hwang and Eaton, 2004). Configurations of the latter type have employed forcing elements such as oscillating grids (Villermaux et al., 1995), speakers (Webster et al., 2004), fans (Birouk et al., 2003), or jets (Krawczynski et al., 2010). The symmetric configuration and (in some cases) the use of random forcing is helpful to reduce mean flow and secondary circulation (Hwang and Eaton, 2004; De Jong et al., 2009). Our method (outlined in Bellani and Variano, 2014) uses randomly forced facing jet arrays to produce a large volume of HI turbulence with a low mean flow and a high Reynolds number.

Each jet array contains 64 pumps mounted on an equally-spaced 8 × 8 Cartesian grid, so that each outflow jet (diameter 2.19 cm) is 10 cm from its neighbors. The two facing arrays of pulsating jets are driven stochastically: both the on- and the off-time for each jet is normally distributed with a known mean and standard deviation, based on the "sunbathing algorithm" outlined in Variano and Cowen (2008). In the center region of the tank, the signatures of the individual jets are no longer discernable, and the turbulence is homogeneous and isotropic. The stochasticity of the firing jets keeps tank-scale mean flow weak, and the symmetry of the two arrays contributes to isotropy. Though some tank-scale circulation is present, it is minimized via this method (Bellani et al., 2012). The tank's working fluid is tap water that has been filtered to 5 microns, and is continuously UV-purified to prevent microbial growth (except when data is being collected). The region of HI turbulence extends over several integral length scales in each

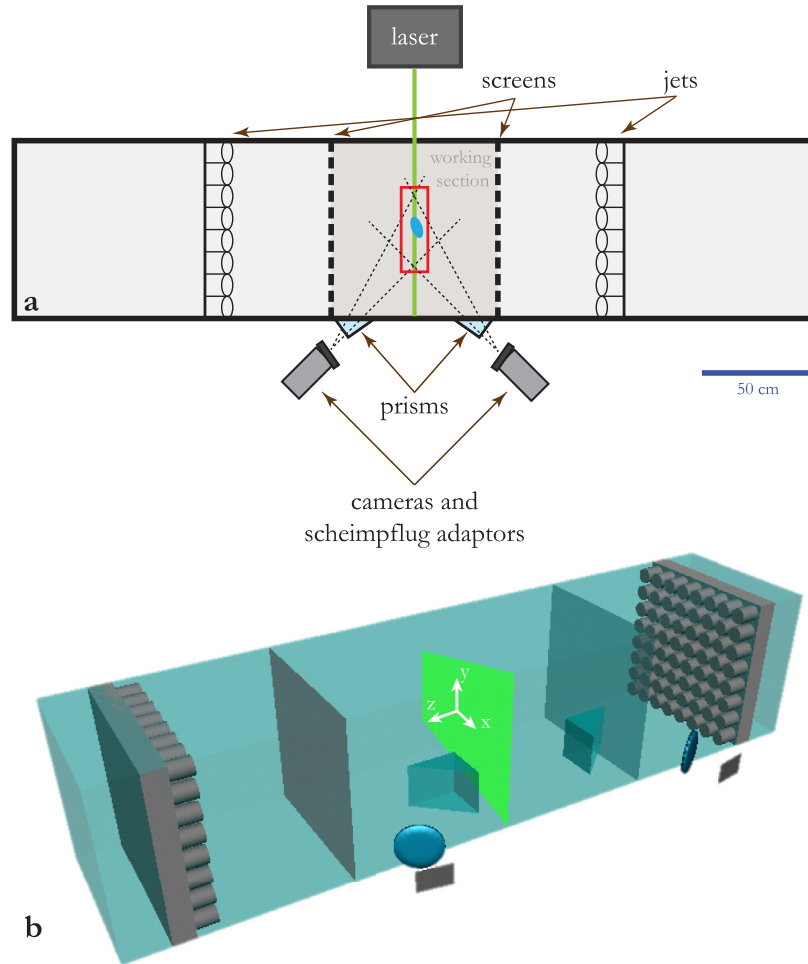


Fig. 1. (a) Turbulence-generating tank, top view (to scale). Turbulence is generated via two facing jet arrays, whose signatures pass through screens to form a central volume of homogeneous isotropic turbulence. Two cameras focus stereoscopically on a two-dimensional central image window. (b) 3-D view of turbulence tank (not to scale), showing jets, screen, laser sheet, prisms, and cameras (stylized as lens and CCD chip).

direction (for a complete characterization of the turbulence within the tank, along with a quantification of the homogeneity and isotropy in the working section, see (Bellani and Variano, 2014)). Due to the large size of the HI region, a cylinder entering the measurement plane necessarily passes through a region of turbulence which is large compared to its own length. Therefore, the motion which we measure is determined primarily by turbulence that is statistically uniform. This is critical for studies of particles in flow due to the influence of the particle's history on its motion at a given time (Reeks and McKee, 1984; Armenio and Fiorotto, 2001).

The tank cross-section is 80 cm \times 80 cm, with a total length of 360 cm. The central working section of the tank is bounded by mesh screens, which prevent the suspended cylinders from being destroyed in the jet intakes and help improve the isotropy of the flow. Each jet panel is 45.5 cm from the mesh screens, and the screens are each 37.5 cm from the central measurement plane. The working section is therefore 75 cm and the total distance between the jets is 166 cm (Fig. 1). This configuration is identical and contemporary to that reported in (Bellani et al., 2013), with identical turbulence properties (summarized in Table 1). In our tank-based coordinate system, the x -direction is the lateral (in-plane, horizontal) direction; the y -direction is the vertical (in-plane, gravity-coupled) direction; and the z -direction is the axial direction, aligned with the jets and out-of-plane in the stereoscopic imaging configuration (Fig. 1). The corresponding velocities are denoted as u , v , and w .

The properties of the turbulence in our facility are comparable to those of small-scale ocean turbulence (Jiménez, 1997; Fuchs and Gerbi, 2016). The Taylor-scale Reynolds number Re_λ , dissipation rate ϵ , turbulent velocity scale u_T , turbulent kinetic energy q^2 , and Kolmogorov microscale η are well within the range that has been measured in the ocean. Therefore, our facility generates turbulence that is statistically similar to that which might be experienced by marine animals or suspended aggregates (one motivator of our study).

2.2. Hydrogel cylinders and refractive index matching

Optical velocimetry techniques such as sPIV are attractive because they are information-rich, allowing the exploration of both one- and two-point fluid statistics. However, for particle-laden flows, the presence of solid objects in the flow handicaps these techniques by creating shadows in the laser plane and/or interfering with the spatial calibration of the PIV algorithm. This problem may be avoided through refractive-index matching between the fluid and solid phases. This allows the laser to pass through particles without distortion, enabling simultaneous measurements of the fluid flow field and the particle kinematics.

We fabricate nonspherical cylindrical particles out of agarose hydrogel, which are refractive index matched to water as outlined in (Byron and Variano, 2013). To make the cylinders, we cast the gel into a sheet of uniform thickness and use thin-walled pipes to

Table 1

Turbulent statistics of experimental facility, where $u_T = \sqrt{\frac{1}{3}(\overline{u^2} + \overline{v^2} + \overline{w^2})}$, $q \equiv \frac{3}{2}u_T^2$, $\epsilon \equiv 30\nu u_T^2 \cdot \lambda_f^{-2}$, $\eta \equiv (\nu^3/\epsilon)^{\frac{1}{4}}$, $\tau_\eta \equiv (\nu/\epsilon)^{\frac{1}{2}}$, $T \equiv L_f \cdot u_T^{-1}$, $Re_\lambda \equiv u_T \cdot \lambda_f \cdot \nu^{-1}$, and $Re_L \equiv u_T \cdot L_f \cdot \nu^{-1}$ (overbars denote time-averaging). Values are compared when possible to corresponding properties of small-scale ocean turbulence as reported in Jiménez (1997). Italicized bracketed intervals represent 95% confidence interval calculated via bootstrapping. All calculations of turbulent statistics are based on (Pope, 2001). We note that the turbulence generated in this facility is not strictly isotropic, as the lateral/vertical vs. axial velocity scales differ slightly from one another; however, this variation is small (less than 15%) and does not appear to influence the results.

Property			Jiménez (1997)	This work	(95% CI)
Lateral velocity scale	$\sqrt{\overline{u^2}}$	$[\times 10^{-2} \text{ m s}^{-1}]$	–	1.97	[1.92, 2.02]
Vertical velocity scale	$\sqrt{\overline{v^2}}$	$[\times 10^{-2} \text{ m s}^{-1}]$	–	≈ 1.97	(by x-y symmetry)
Axial velocity scale	$\sqrt{\overline{w^2}}$	$[\times 10^{-2} \text{ m s}^{-1}]$	–	2.29	[2.20, 2.36]
Turbulent velocity scale	u_T	$[\times 10^{-2} \text{ m s}^{-1}]$	1–3	2.08	[1.99, 2.17]
Kinematic viscosity	ν	$[\times 10^{-7} \text{ m}^2 \text{ s}^{-1}]$	–	8.93	–
Turbulent kinetic energy	q^2	$[\times 10^{-4} \text{ m}^2 \text{ s}^{-2}]$	2–14	6.47	[6.21, 6.77]
Turbulent dissipation rate	ϵ	$[\times 10^{-5} \text{ m}^2 \text{ s}^{-3}]$	0.01–10	4.95	[4.72, 5.16]
Taylor microscale	λ_f	$[\times 10^{-2} \text{ m}]$	–	1.33	[1.12, 1.57]
Integral lengthscale	L_f	$[\times 10^{-2} \text{ m}]$	–	8.3	[8.1, 8.9]
Kolmogorov lengthscale	η	$[\times 10^{-3} \text{ m}]$	0.03–0.2	0.50	[0.42, 0.52]
Kolmogorov timescale	τ_η	[s]	–	0.13	[0.12, 0.14]
Eddy turnover time	T	[s]	–	3.9	[3.7, 4.1]
λ_f -based Reynolds number	Re_λ	–	200–1000	310	[260, 382]
L_f -based Reynolds number	Re_L	–	–	1936	[1914, 2012]

Table 2

Dimensions (height, diameter, aspect ratio, volume, and surface area) of the four types of hydrogel cylinders studied herein. Across the four types, volume varies by no more than 21% around a mean of 0.415 cm³; surface area varies by no more than 5% around a mean of 3.30 cm². Errors marked are twice the standard error, representing 95% confidence interval.

$H = 2c$ (mm)	$D = 2a = 2b$ (mm)	$\alpha = \frac{c}{a}$ (–)	V (cm ³)	S.A. (cm ²)
4.77 ± 0.22	10.60 ± 0.26	0.45	0.421	3.35
8.24 ± 0.36	8.72 ± 0.94	0.94	0.492	3.45
12.99 ± 0.28	6.41 ± 0.22	2.02	0.419	3.26
18.91 ± 0.12	4.70 ± 0.08	4.02	0.328	3.14

cut out cylinders of varying aspect ratios, with known height $2c$ (gel sheet thickness) and known diameter $2a$ (inner diameter of pipe). We can therefore calculate cylinder aspect ratio $\alpha \equiv \frac{c}{a}$. During manufacturing, we embed small (13–44 μm) glass spheres into the cylinders (Cataphote Inc., Flowood, MS; Class 4a, size 3200). These spheres act as tracers, so that the sPIV algorithms used to calculate the fluid velocity field may also be used to calculate the velocity field of a planar slice through the cylinder. This measured solid-body velocity field allows us to calculate the cylinder's angular velocity as well as a representative translational velocity (see Section 2.4). The hydrogel scatters slightly more light than the surrounding fluid, allowing the cylinder slice to be isolated via basic image processing. Vector computation (via sPIV) is performed separately on the separated solid and fluid phases.

We fabricate agarose cylinders at four different aspect ratios (α) logarithmically ranging from 0.5–4 (Table 2). To explore the effect of small density variations near neutral buoyancy, we use two concentrations of agarose: 0.4% and 0.8% by mass, corresponding to cylinder specific gravities of $SG_1 = 1.003$ and $SG_2 = 1.006$ red (where specific gravity was measured after the addition of the hollow glass tracers, so that these measurements represent the cylinders and not the unadulterated hydrogel). This results in eight independent cylinder types (four aspect ratios and two densities, both close to neutral buoyancy). In all experiments, cylinders are added (by type) to the turbulence tank's working section at a volume fraction $\Phi = 0.1\%$. This volume fraction ensures that cylinders regularly pass through the image window, but that cylinder-cylinder collision is infrequent (Elghobashi, 1994).

2.3. Stereoscopic particle image velocimetry

Suspended cylinders are stereoscopically imaged, simultaneously with the surrounding fluid, using two CCD cameras (Imager PRO-X, 1600 × 1200 pixels, with 105 mm Nikkor lens and Scheimpflug/tilt adapter). Each camera is equipped with a polarizing filter to increase the contrast between the embedded tracers and the hydrogel. Polarizer alignment is set to maximize this contrast. The two CCD cameras focus on opposite sides of the laser light sheet (Fig. 1), separated by 110°. The resultant test section is a 75 mm × 35 mm area in the center of the homogeneous and isotropic region of the tank. To minimize interfacial distortion, cameras view the test section through 35° water-filled acrylic prisms. The test section lies within a 1 mm-thick laser sheet (Quantel/Big Sky Lasers, 532 nm) which bisects the tank (Fig. 1). Flow is seeded with 11 μm neutrally buoyant glass spheres (Spherul 110P8, Potters Industries). Image pairs are collected at a frame rate of 14.773 Hz, with a 4 ms separation between successive images. No timeseries data were considered in this study; independent identically distributed vector fields are computed from the collected image pairs.

Multipass sPIV computation was performed using a commercial software package (DaVis 7, Lavisio GmbH; Goettingen, Germany), using multipass PIV from 128 × 128 to 64 × 64 pixel interrogation windows with 50% overlap. For the interior vector fields, additional image preprocessing tools (sliding background subtraction and particle normalization) are used to identify the tracers within the hydrogel cylinders. The resulting vector field represents an average of the fluid flow over a square window of side length 2.6 mm, and a vector is calculated every 1.3 mm. These length-scales are only slightly larger than the Kolmogorov scale ($\eta = 0.5 \text{ mm}$) and are small compared both to the cylinders and to the Taylor microscale.

2.4. Kinematic analysis

We collect a large number of independent measurements of cylinders in flow ($N = 101 - 413$), with each measurement including both the interior (cylinder) vector field and exterior (fluid) vector field, collected simultaneously. From these data, we seek to calculate two vector-valued quantities: a representative cylinder translational velocity \mathbf{u}_p and a representative fluid velocity \mathbf{u}_f .

Differences in sample size reflect differences in the overall difficulty of measurement, including both variation in the cylinder fabrication process (to achieve the desired aspect ratio) and differences in the rate of cylinders passing through the observation window. Because of the low volume ratio (held constant at $\Phi = 0.001$), cylinders were regularly but infrequently observed passing through the image window. This resulted in an experimental time of several hours, with multiple trials run over several days to achieve the necessary statistical power. This combination of non-trivial experiment scheduling, together with variations in the “hit rate” through the image window, led to the differences in sample size. However, no differences were observed in the process of data analysis between relatively large and small sample sizes (see Table A.1).

2.4.1. Planar approximation of slip velocity

As discussed in 1.1, slip velocity may be defined as:

$$\mathbf{u}_s \equiv \mathbf{u}_p - \mathbf{u}_f \quad (2)$$

where \mathbf{u}_p is the cylinder velocity and \mathbf{u}_f is the fluid velocity that would have been measured at the cylinder center if the cylinder itself was not present. In an experimental context, \mathbf{u}_f is impossible to measure directly and must be inferred. We therefore choose to define \mathbf{u}_f as the average velocity within a two-dimensional annulus surrounding the in-plane cylinder slice. We choose the inner boundary of this annulus to be as close to the cylinder as possible without including the immediately-adjacent vectors (which may still strongly include the cylinder's influence due to the no-slip boundary condition and/or particle-induced fluid motion). We choose the outer boundary of the annulus to be a distance of $D_s = 9.2$ mm (the volume-equivalent sphere diameter) from the edge of the cylinder slice. The presence of viscosity ensures that a nontrivial volume of fluid is pulled along with the cylinder (Darwin, 1953). However, at the studied Reynolds numbers ($50 < Re < 350$), this volume does not extend very far from the cylinder except in a comparatively narrow wake region, even in quiescent flow (Katija and Dabiri, 2009). The presence of turbulent structures is likely to further disrupt the drift volume, so that the annulus is unlikely to contain a significant proportion of fluid affected by particle-induced drift. To further confirm this, a sensitivity analysis also showed minimal response to varying the annulus bounds. The fluid velocity \mathbf{u}_f is therefore defined to be the average velocity within the bounding annulus, and the cylinder velocity \mathbf{u}_p is defined to be the average velocity of the in-plane cylinder slice.

Since our measurement method includes only a two-dimensional slice of the velocity field in both the fluid and solid phases, we must consider potential bias in our results. If the cylinder is rotating, the in-plane slice may be moving in a different direction than the cylinder's actual center of mass; in fact, it is unlikely that the cylinder center of mass is in the laser plane at all. However, Bellani and Variano (2012) showed that for this and similar cases, this “rotation-induced noise” is on the order of 0.1% when compared to the overall cylinder velocity, and may therefore be neglected. We further expect that since the turbulence is homogeneous and isotropic, any error introduced via this method will be random, not bias error, and thus cancel to zero when cylinder velocity statistics are calculated.

2.4.2. Quiescent cylinder settling

To measure their settling velocity in still water (v_q), hydrogel cylinders are released at the top of a hexagonal water-filled tank of 500 mm vertical extent (Fig. 2). One face of the tank is overlaid with an opaque plate, with 2 mm-wide slits laser-cut at 50 mm intervals. Two handheld lasers (Wicked Lasers, Hong Kong), both fitted with screw-in sheet optics, are mounted on a ring stand

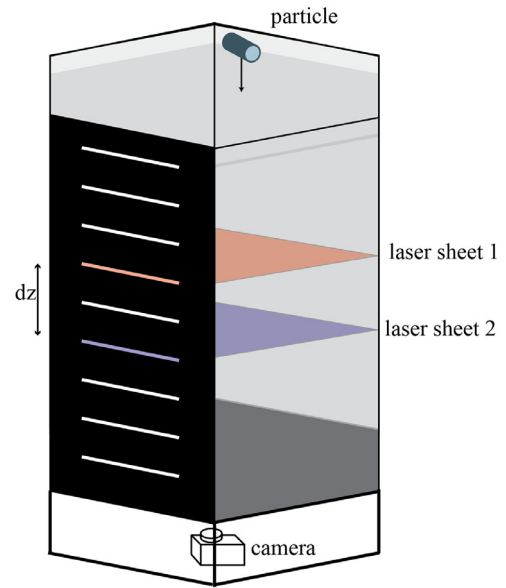


Fig. 2. Setup for measuring quiescent settling velocity of hydrogel cylinders. Two laser sheets are placed at a known distance dz . A camera films from below, measuring the time dt as the cylinder passes through the two sheets. The settling velocity is dz/dt . The process is repeated throughout the vertical extent to find the terminal settling velocity.

Table 3

Cylinder terminal (quiescent) settling velocities v_q and Reynolds number $Re_q = \frac{v_q L}{\nu}$, where L is a representative lengthscale (brackets show Re_q calculated using shortest and longest cylinder length; unbracketed Re_q is calculated using the diameter of a volume-equivalent sphere. Cylinders are listed by aspect ratio α and specific gravity SG.

α (-)	SG (-)	v_q (cm/s)	Re_q (-)
0.5	1.003	-1.47 ± 0.14	153 [79, 175]
1	1.003	-1.34 ± 0.10	147 [123, 130]
2	1.003	-1.10 ± 0.10	114 [78, 160]
4	1.003	-0.98 ± 0.09	95 [52, 207]
0.5	1.003	-1.59 ± 0.16	166 [85, 189]
1	1.003	-2.48 ± 0.17	272 [229, 242]
2	1.003	-1.65 ± 0.16	172 [118, 240]
4	1.003	-1.64 ± 0.13	157 [86, 347]

and positioned such that the laser planes are parallel, horizontal and shining directly through two of the precision-cut slits. A digital camera (Nikon J1; Nikon Corporation, Tokyo, Japan) views the tank from below through the transparent tank floor, filming at 60 frames per second. A clearly-delineated short flash of light indicates the time at which the cylinder passes through the two laser planes. By positioning the two laser planes at a known vertical interval Δz , and observing the time interval Δt between the measured flashes, the average settling velocity over the interval may be calculated as $\Delta z/\Delta t = v_q$. To determine the terminal settling velocity, the experiment is repeated over several vertical intervals, starting near the top of the tank and progressing downwards until a steady-state terminal velocity is achieved (Table 3).

3. Results and discussion

3.1. Effects of gravity on slip velocity

Fig. 3 shows a component-wise plot of \mathbf{u}_p vs. \mathbf{u}_f for a large number of independent fluid-cylinder measurements (each panel represents one of the eight cylinder types). The one-to-one limit,

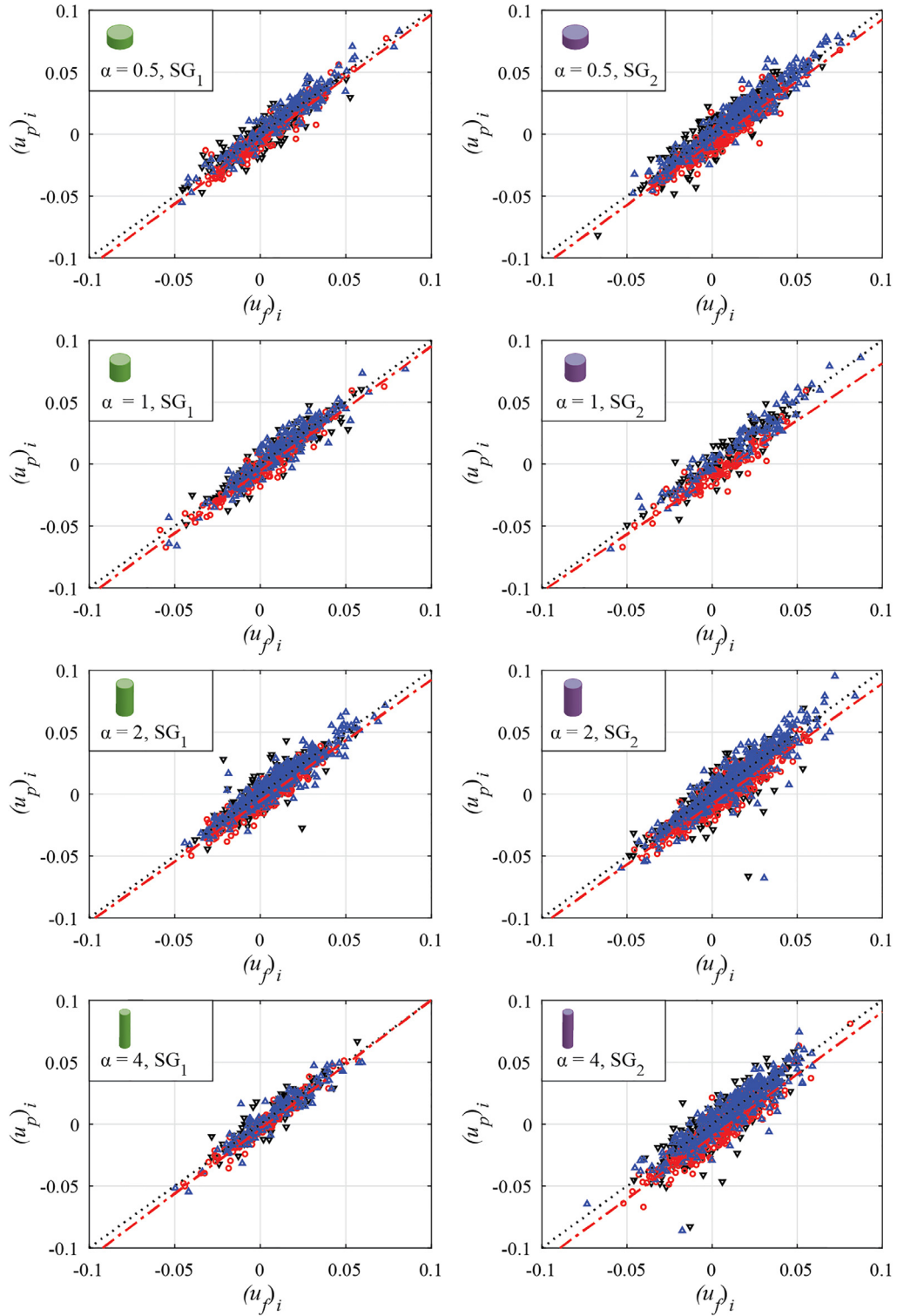


Fig. 3. Cylinder velocity \mathbf{u}_p vs. fluid velocity \mathbf{u}_f , plotted component-wise. Point-down black triangles (∇) represent the x-component u ; red circles (\circ) represent the y-component v ; point-up blue triangles (Δ) represent the z-component w . Small-dashed black line indicates the one-to-one limit in which $\mathbf{u}_p = \mathbf{u}_f$. Dash-dot red line represents the linear best-fit trend for the y-component v_p vs. v_f . (For interpretation of the references to colour in this figure legend, the reader is referred to the web version of this article.)

where $(u_p)_i = (u_f)_i$, is shown as the black dotted line in Fig. 3). The lateral velocities u and w cluster about this line, whereas the vertical velocity v is linearly offset below (indicative of the influence of gravity, which is stronger for the heavier cylinders). All three components can be reasonably described with a linear trend (for the vertical component, v , this is shown as the red dash-dot

line in Fig. 3); parameters for all fits are given in Table A.2. Some scatter occurs because the cylinders are inertial, with \mathbf{u}_p diverging from \mathbf{u}_f (non-zero slip velocity). However, since the ambient turbulence is homogeneous and isotropic, the ensemble-averaged slip velocity should be zero in all but the vertical component. To further develop this idea, we introduce the following useful

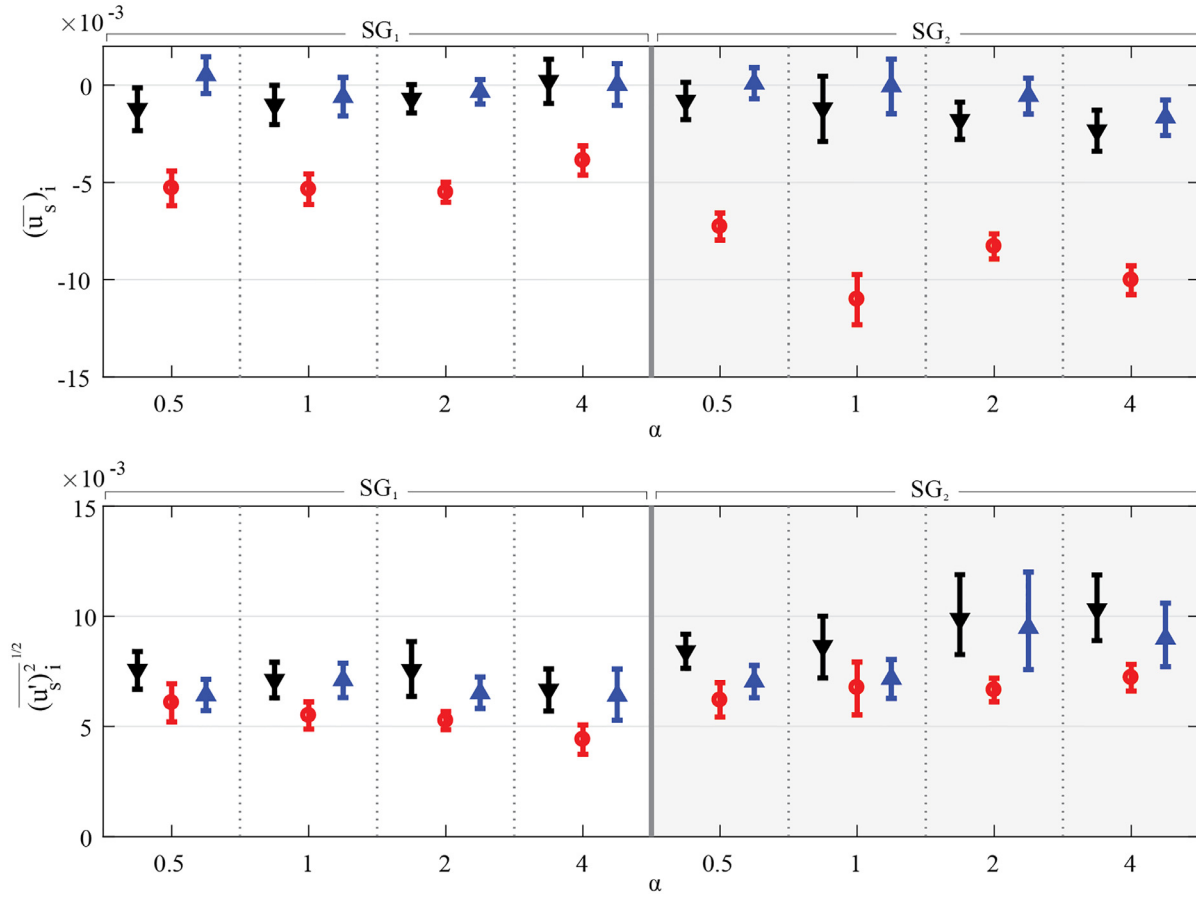


Fig. 4. Decomposition of the slip velocity, displaying the components of both $\bar{\mathbf{u}}_s$ and $(\bar{\mathbf{u}}_s'^2)^{1/2}$ in meters per second. For $\bar{\mathbf{u}}_s$ (top panel), the y-component \bar{v}_s (red circles, \circ) is significantly lower than the horizontal x-component \bar{u}_s (black point-down triangles, ∇) or z-component \bar{w}_s (blue point-up triangles, \triangle), both of which are near zero. \bar{v}_s is lower for cylinders with a higher specific gravity, indicative of gravitational settling. For $\bar{\mathbf{u}}_s'^2$ (bottom panel), the vertical component $\bar{v}_s'^2$ is slightly lower than the horizontal components $\bar{u}_s'^2$ and $\bar{w}_s'^2$. On average, slip is higher for cylinders with higher specific gravity. Error bars represent 95% confidence intervals, calculated via bootstrapping with 1000 replicates. (For interpretation of the references to colour in this figure legend, the reader is referred to the web version of this article.)

decomposition of the slip velocity:

$$\mathbf{u}_p - \mathbf{u}_f = \mathbf{u}_s = \bar{\mathbf{u}}_s + \mathbf{u}_s' \quad (3)$$

where the overbar represents ensemble averaging over a large number of independent measurements. $\bar{\mathbf{u}}_s$ is therefore the average of many independent measurements of \mathbf{u}_s , and \mathbf{u}_s' is the instantaneous fluctuation about $\bar{\mathbf{u}}_s$. Because the turbulence is homogeneous and isotropic, we expect the lateral components \bar{u}_s and \bar{w}_s to be zero. The instantaneous fluctuations, \mathbf{u}_s' , capture all the effects of cylinders' Lagrangian histories as well as any measurement noise. \mathbf{u}_s' therefore can be called the “true slip”: the part of $\bar{\mathbf{u}}_s$ which is left over after gravitational settling has ostensibly been removed. A higher instantaneous value of \mathbf{u}_s' corresponds to a greater departure from a one-to-one relationship between \mathbf{u}_f and \mathbf{u}_p , shown by the black dotted lines in Fig. 3.

Fig. 4 shows values of $\bar{\mathbf{u}}_s$ and $(\bar{\mathbf{u}}_s'^2)^{1/2}$ derived from the measurements shown in Fig. 3. From these two figures, we call attention to two salient features. One, the vertical (gravity-coupled) component of $\bar{\mathbf{u}}_s$ is nonzero for all cylinder types (such that $\bar{v}_s \neq 0$), whereas \bar{u}_s and \bar{w}_s are approximately zero (see Table A.1), as expected. Two, it is apparent from Fig. 3 that $(u_p)_i$ are well-described as linear functions of $(u_f)_i$; the slope of this linear dependence is approximately one for all velocity components, regardless of the cylinder aspect ratio α or cylinder specific gravity (see Table A.2). When examining the decomposition between $\bar{\mathbf{u}}_s$ and \mathbf{u}_s' (Fig. 4), the effect of cylinder specific gravity is apparent. More massive cylinders have higher \bar{v}_s , indicating stronger gravitational settling. More

massive cylinders also have higher $(\bar{\mathbf{u}}_s'^2)^{1/2}$, on average, across all dimensional components. This is not surprising, as the more massive cylinders have more inertia and are expected to have higher slip velocity. The average “true slip” $\bar{\mathbf{u}}_s' = 0$ by definition (see Eq. (3)). However, $\bar{\mathbf{u}}_s'^2 \neq 0$ in general.

Gravity plays a role in determining $\bar{\mathbf{u}}_s$ as well as $\bar{\mathbf{u}}_s'$. For both tested specific gravities, $\bar{v}_s'^2$ is slightly smaller than the horizontal components $\bar{u}_s'^2$ and $\bar{w}_s'^2$. This indicates that the effects of gravity do not entirely disappear, even when they have ostensibly been removed from the overall slip velocity. The presence of gravity contributes not only to cylinder settling, but anisotropically alters the “true slip” velocity in such a way that the variance of \mathbf{u}_s in y is less than the variance in x and z. This effect is visible even though the cylinders are very close to neutrally buoyant. We can conclude that small changes in buoyancy play a more pronounced role in large-particle dynamics than has been previously considered, and that large nearly neutrally buoyant particles may sample the flow anisotropically even if the ambient turbulence is isotropic.

3.2. Comparison to single-phase fluid velocity

Fig. 5 shows the probability density function for the turbulent velocity fluctuations u' , v' , and w' as measured in the unladen (background) turbulence. It is compared to a normalized histogram of the observed cylinder velocities. Because the cylinders are one to two orders of magnitude larger than the Kolmogorov scale, they may be expected to spatially filter the small-scale structures, so

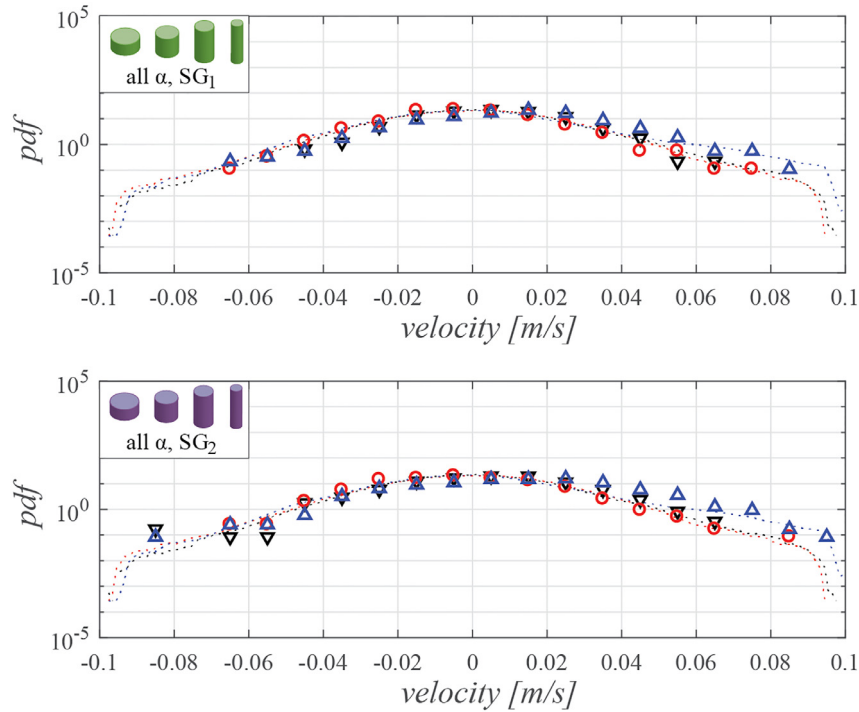


Fig. 5. Probability density functions of the single-phase (unladen) fluid velocity (dotted lines), overlaid with a normalized histogram of observed cylinder velocities. Here, black lines/markers represent the x-component u , red lines/markers represent the y-component v , and blue lines/markers represent the z-component w . Markers used to denote cylinder velocity histogram are point-down triangles (u), circles (v), and point-up triangles (w). Here we have combined all shapes to increase the number of samples available for the histogram and thereby decrease the effect of outliers; the same data, separated by aspect ratio and plotted using the same bin size, are available in Fig. A.1. Despite their large size, cylinders do not appear to filter the small-scale fluid structures; their velocity distribution is similar to that of the unladen fluid velocity. (For interpretation of the references to colour in this figure legend, the reader is referred to the web version of this article.)

that they do not “feel” the small-scale intermittency of the ambient turbulence. However, we find that this is not the case. The cylinder velocity distribution, perhaps surprisingly, is comparable to that of the single-phase fluid velocity. If anything, the cylinder velocity distribution is slightly wider than the fluid velocity distribution, indicating that relatively large cylinder velocities are more common than fluid velocities of the same magnitude. These data suggest that some kind of preferential concentration or sampling is at work.

One possibility that would result in these observations is *preferential concentration*. High cylinder velocities are equally represented (or perhaps over-represented) compared to high fluid velocities. When the effect of spatial filtering is considered— a physically reasonable inference— these high velocities are certainly over-represented. Since the cylinders extract kinetic energy from the fluid turbulence, and from no other source, the only way for a large cylinder to achieve a high absolute velocity would be for it to be embedded in a high-velocity fluid region with very little slip. This suggests that the large cylinders are preferentially concentrated in high-velocity zones. While our data cannot directly explore this potential mechanism, we can examine it indirectly by looking more closely at the slip velocities shown in Fig. 3 across the entire range of observed velocities. We find that \mathbf{u}_p is *more closely correlated* with \mathbf{u}_f in the extremes of the dataset: the correlation coefficient between \mathbf{u}_p and \mathbf{u}_f is substantially higher for the first and fourth quartiles of observed \mathbf{u}_f than for the second and third quartiles (see Table A.3). This observation is true for all aspect ratios and specific gravities studied. However, it is unclear what mechanism would preferentially concentrate large cylinders in high-velocity zones.

A subtle subcategory of this hypothesis is that high-velocity cylinders are *preferentially sampled* due to experimental constraints: That is, they may not preferentially occur in regions of high fluid velocity in general, but when they do, they are more

likely to pass through the measurement window. This is a potential consequence of our sampling method: since we observe cylinders whenever they pass through the measurement window, fast-moving cylinders may be seen more often than slow-moving ones. We discuss this possibility further in Section 3.3 below. In any case, further work is necessary to understand the mechanism(s) behind this interesting phenomenon.

3.3. Possible effects of resuspension

All measurements in this study took place in the central region of the tank, where the turbulence was measured to be nearly homogeneous and isotropic with zero mean flow. However, as stated in Section 1.2, the boundedness of the vessel ensures that the suspended cylinders will encounter non-homogeneous regions. These non-homogeneous regions are well outside the measurement area: cylinders will pass through several integral lengthscales before entering the measurement window, thus minimizing any effects due to history. However, the presence of walls (even far outside the measurement window) may still drive differences in our measurements relative to the idealized case of unbounded H.I. turbulence. For example, consider that the cylinders we study are slightly negatively buoyant and sized within the inertial range. In unbounded turbulence, the cylinders’ vertical displacement would also increase without bound. In our experiment, the cylinders rest on the bottom of the tank for some period of time until a gust arises which is strong enough to lift them back into the flow, where they may again pass through the measurement window. A simple thought experiment reveals the following: 1) Resuspension requires a relatively strong upward gust to lift the cylinders from the bottom; 2) due to its strength, the cylinders may remain in that gust for some time; 3) if these resuspended cylinders reach the measurement window, they are likely to exhibit a lower-in-magnitude vertical slip velocity than cylinders which have

remained suspended without contacting the bottom. If enough of these resuspended cylinders are measured (i.e., if the experiment proceeds for a long time), it may contribute to an average decrease in the vertical component of the slip (but not the horizontal components). This is in fact what we see. However, this hypothesis is not directly testable with our current data.

The above discussion refers to *experimental constraints* related to the presence of resuspension. However, there may also be *physical mechanisms* that lead to resuspension, which would be present even in unbounded turbulence. For example, the vortex-trapping mechanism presented by Tooby et al. (1977) was found to be present for large particles, rather than the “fast-tracking” observed by others (Maxey and Corrsin, 1986; Maxey, 1990). This mechanism would lead large particles to remain suspended longer than smaller particles with the same specific gravity. However, the fast-tracking mechanism has typically been observed only with heavy particles, so it is unclear how the dichotomy between vortex-trapping and fast-tracking would apply at near-neutral buoyancy (if it applies at all). For this reason we believe that the experimental constraints discussed above are a more likely explanation for our observations. However, further exploration of the parameter space (both size and specific gravity) are needed to clarify the physical mechanisms at play.

3.4. Possible effects of shape

No significant effects due to shape variation are observed in the “true slip” \mathbf{u}'_s (see Fig. 4). This is perhaps surprising, as aspect ratio has been shown to impact particle rotation and alignment in turbulent flows (Parsa et al., 2012; Byron et al., 2015). However, these cylinders are large compared to most in the literature, and their aspect ratios are relatively close to one. If there is an effect of aspect ratio in this small section of the parameter space, it is subtle and not detectable with our experiments. Further treatment, perhaps computational in nature in order to sweep out a wider and more resolved range of aspect ratios, may be required to elucidate the effects of shape here.

However, further examination of Fig. 4 hints that shape may affect the turbulence-altered settling velocity \bar{v}_s . No shape effects are apparent for the lighter cylinders (SG₁). However, for the heavier (SG₂) cylinders, a trend emerges that follows the quiescent settling velocities listed in Table 3. For $\alpha = 1$ in still water, the heavier cylinders settle unusually quickly—about 150% faster than the other three cylinder types with the same density. The difference is significant. In turbulence, the $\alpha = 1$ case also shows a lower (faster) value of \bar{v}_s than the other cylinders of the same density. This difference is also significant and of the same order of magnitude as that observed in the quiescent case. A slightly enhanced \bar{v}_s is also visible in the turbulent $\alpha = 4$ case.

We hypothesize two possible explanations for this observation. First, for quiescent settling, the $\alpha = 1$ case presents the lowest cross-sectional area; it will therefore experience a lower drag force and a correspondingly higher terminal velocity. In turbulence, the $\alpha = 1$ case is closest to spherical, and the average cross-sectional diameter encountered by the flow is smaller than other aspect ratios even if orientation is completely random (which we cannot claim). However, this fact should potentially drive shape-dependent differences in \mathbf{u}'_s , which we do not see. Second, it is possible that the relationship between cylinder behavior and aspect ratio in this region of the parameter space is highly non-linear. We have recently conducted similar experiments which support this claim (Angle et al., 2019), attributing differences in settling behavior to possible instabilities in the cylinder wake. In either case, further study is needed to elucidate the role of aspect ratio on turbulence-altered settling and slip for large particles.

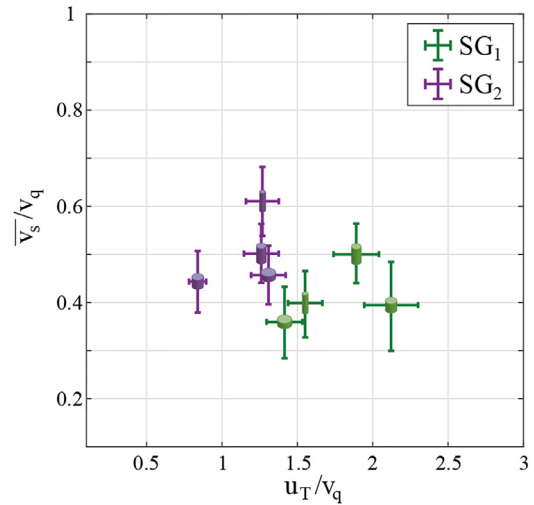


Fig. 6. Relative settling velocity \bar{v}_s/v_q vs. turbulence strength u_T/v_q . Though both densities experienced significantly reduced settling, SG₁ was reduced more than SG₂. Errorbars represent 95% confidence interval, calculated via bootstrapping. Green symbols represent the lighter cylinders, and purple symbols represent the heavier cylinders. (For interpretation of the references to colour in this figure legend, the reader is referred to the web version of this article.)

3.5. Comparison to quiescent settling

We compare \bar{v}_s to the measured quiescent settling velocity, v_q . Fig. 6 shows the relative settling velocity, \bar{v}_s/v_q , as a function of the relative turbulence strength, u_T/v_q (where u_T , the turbulent velocity scale, is a constant property of the flow listed in Table 1). The relative turbulence strength quantifies how the turbulence is “felt” by the cylinders: A cylinder with high specific gravity, with a correspondingly high quiescent settling velocity v_q , would have $u_T/v_q \rightarrow 0$ and pass through turbulence relatively unaffected. A cylinder with $u_T/v_q > 1$ would result in a reduced relative settling velocity. This analysis has been performed for a few classes of relatively small particles (at or below the Kolmogorov scale), showing that $\bar{v}_s/v_q \rightarrow 0$ for particles with $u_T/v_q > 1$ (Nielsen, 2007). However, large particles of the type we consider here are not as well-studied.

Fig. 6 shows that the turbulent settling velocity \bar{v}_s is significantly reduced compared to the quiescent settling velocity v_q , with \bar{v}_s around or less than 50% of v_q for all cylinder types. Again, there is no significant effect of shape, but a small effect of specific gravity, with SG₁ experiencing a stronger reduction in settling velocity than SG₂. This is logical, since the relative turbulence strength is smaller for the more massive cylinders, moving them toward the known point where $v_q = \bar{v}_s$ at $u_T = 0$. We may additionally assume that as the turbulence strength increases, \bar{v}_s will asymptotically approach zero. Our data are consistent with these known extreme behaviors.

4. Conclusions

Using stereoscopic PIV and refractive index matching, we have measured the slip velocity $\mathbf{u}_s \equiv \mathbf{u}_p - \mathbf{u}_f$ for near-neutrally buoyant cylinders at four aspect ratios and two mass densities, whose lengths are close to the Taylor lengthscale of the ambient turbulence. From these data, we calculated several quantities of interest: 1) The average slip, $\bar{\mathbf{u}}_s$; 2) the “true slip”, \mathbf{u}'_s ; and 3) the relative settling velocity \bar{v}_s/v_q . These are compared by relative turbulence strength u_T/v_q , density, and shape.

We find that the instantaneous cylinder velocity \mathbf{u}_p is well-predicted by the surrounding instantaneous fluid velocity \mathbf{u}_f , with some variation around a one-to-one relationship: scatter,

indicating instantaneous slip velocity \mathbf{u}'_s , and offset, indicating average slip $\overline{\mathbf{u}}_s$ (where $\mathbf{u}_s \equiv \overline{\mathbf{u}}_s + \mathbf{u}'_s$). In general, \mathbf{u}_p is more closely correlated to \mathbf{u}_f at the extremes of the dataset. This is also borne out in the overall cylinder velocity distribution, which is close to the single-phase fluid velocity distribution. Since the cylinders are inertial, this result is surprising; the cylinders should pass through intermittent high-velocity events without equilibrating to the surrounding velocity, filtering out the small-scale fluctuations. This result may indicate some preferential concentration effects, in which cylinders remain within areas of high fluid velocity for longer than expected. It may also be a consequence of experimental constraints.

We do not observe any effect of shape in any of the calculated quantities for the more neutrally buoyant cylinders (SG₁). For the slightly denser cylinders (SG₂), a small effect on \overline{v}_s may be present at aspect ratio $\alpha = 1$; we attribute this to potential differences in the average cross-sectional area presented to the flow, as was evident in measurements of the quiescent settling velocity v_q (see Table 3). This in turn may affect hydrodynamic drag, and alter the overall slip velocity. Such effects would be more easily observed in the more-inertial cylinders, as we see here.

We find that gravitational effects are important; gravity does not simply add a constant vertical slip to the cylinders. When the average vertical slip is removed, the effect of gravity is still present; for the rms “true slip” $\overline{u_s'^2}^{1/2}$, the vertical component differs (in most cases significantly) from the two horizontal components. This again may indicate preferential sampling of flow gradients in the history term, so that the slip velocity is anisotropic even though the ambient turbulence is isotropic. This has significant implications for the study of large particles in turbulence, as it indicates that the slip velocity cannot be assumed to be isotropic even for particles which are very close to neutral buoyancy. It also invites further investigation of longer particle trajectories together with the surrounding flow, which will show whether particles preferentially sample updrafts vs. downdrafts, as illustrated in

previously observed mechanisms such as vortex trapping and fast tracking. An alternative mechanism for the observed anisotropy in the slip velocity may be related to particle resuspension, as discussed in Section 3.3.

Lastly, we find that the average vertical slip velocity \overline{v}_s is significantly reduced with respect to the quiescent settling velocity v_q , and that cylinders which are closer to neutral buoyancy experience a greater relative reduction in settling. As the cylinders gain mass, they become less affected by the surrounding turbulence, such that in the limit of very massive cylinders (or very weak turbulence) we expect \overline{v}_s to approach v_q and for very strong turbulence, we expect \overline{v}_s to approach zero. While the mechanisms behind settling-velocity reduction near neutral buoyancy for nonspherical particles remain unclear, they may also have to do with preferential concentration and/or anisotropic sampling of the turbulence.

Future experiments will target potential preferential concentration effects in large nonspherical particles, as these may be responsible for the observed patterns in the slip velocity as well as the reduced settling velocity.

Acknowledgments

The authors gratefully acknowledge funding from NSF DGE 1106400 as well as NSF IGERT 0903711. We thank Ankur Bordoloi, Nimish Pujara, and Colin Meyer for productive discussions, and two anonymous reviewers for their analysis suggestions.

Appendix A. Fit parameters and further calculations of slip velocity

Table A.1 below shows the values, with confidence intervals, of the rms “true slip” velocity and its components, with 95% confidence intervals (these data are plotted in Fig. 4). Cylinder types for which the vertical “true slip” is significantly larger than the horizontal “true slip”, as determined by confidence interval overlap, are marked. Table A.2 gives the fit parameters for the best-fit lines

Table A.1

rms values of \mathbf{u}'_s for all cylinder types and dimensions. Bracketed intervals indicate 95% confidence interval calculated via bootstrapping with 1000 replicates. Cases in which $(\overline{u_s'^2})^{1/2}$ departs significantly (non-overlapping confidence intervals) from the horizontal components are marked with an asterisk.

	α	$(\overline{u_s'^2})^{1/2}$		$(\overline{v_s'^2})^{1/2}$		$(\overline{w_s'^2})^{1/2}$		$(\overline{u_s'^2 + v_s'^2 + w_s'^2})^{1/2}$	
		[$\cdot 10^{-3}$ m s ⁻¹]		[$\cdot 10^{-3}$ m s ⁻¹]		[$\cdot 10^{-3}$ m s ⁻¹]		[$\cdot 10^{-3}$ m s ⁻¹]	
SG ₁	0.5	7.6	[6.7, 8.4]	6.1	[5.2, 6.9]	6.4	[5.7, 7.1]	11.6	[10.6, 12.6]
	1	7.1	[6.4, 7.9]	5.5*	[4.9, 6.1]	7.1	[6.3, 7.9]	11.4	[10.6, 12.4]
	2	7.5	[6.4, 7.9]	5.3*	[4.9, 5.7]	6.5	[5.8, 7.3]	11.3	[10.2, 12.5]
	4	6.7	[5.7, 7.6]	4.4*	[3.7, 5.1]	6.4	[5.3, 7.6]	10.2	[9.2, 11.3]
SG ₂	0.5	8.4	[7.6, 9.2]	6.2	[5.4, 7.0]	7.0	[6.3, 7.8]	12.6	[11.7, 13.5]
	1	8.6	[7.2, 10.0]	6.8	[5.6, 8.0]	7.2	[6.3, 8.0]	13.1	[11.7, 14.5]
	2	9.9	[8.3, 11.9]	6.7*	[6.1, 7.2]	9.5	[7.6, 12.1]	15.2	[13.1, 18.1]
	4	10.3	[8.9, 11.9]	7.2	[6.6, 7.8]	9.0	[7.7, 10.6]	15.5	[13.9, 17.5]

Table A.2

Linear regression parameters for \mathbf{u}_p regressed to \mathbf{u}_f , where R^2 is the coefficient of determination and m is the fitted slope listed with 95% confidence intervals (calculated via bootstrapping). R^2 values range from 0.74 to 0.94, indicating that the data are well-described by a linear model; slopes range from 0.93 to 1.02, indicating that \mathbf{u}_p maps directly to \mathbf{u}_f (barring instantaneous slip \mathbf{u}'_s and measurement noise) across the range of fluid velocities measured. No differences were observed in the fitting process between relatively small sample sizes ($N = 101$) and relatively large sample sizes ($N = 413$).

	α	N	x			y			z		
			R^2	m	95%CI	R^2	m	95%CI	R^2	m	95%CI
SG ₁	0.5	185	0.83	0.93	[0.86, 0.99]	0.91	1.02	[0.96, 1.07]	0.92	1.00	[0.96, 1.05]
	1	192	0.87	0.98	[0.92, 1.04]	0.93	1.01	[0.97, 1.05]	0.90	1.02	[0.96, 1.08]
	2	412	0.77	0.95	[0.89, 1.00]	0.93	0.98	[0.94, 1.02]	0.89	0.96	[0.92, 1.00]
	4	133	0.84	0.98	[0.90, 1.06]	0.94	1.04	[0.99, 1.10]	0.90	0.99	[0.92, 1.04]
SG ₂	0.5	303	0.84	1.01	[0.95, 1.06]	0.90	1.00	[0.96, 1.04]	0.93	1.00	[0.97, 1.03]
	1	101	0.85	1.00	[0.93, 1.08]	0.89	0.92	[0.83, 0.99]	0.93	1.01	[0.95, 1.06]
	2	413	0.73	0.95	[0.90, 1.01]	0.89	0.97	[0.94, 1.01]	0.86	1.02	[0.98, 1.06]
	4	369	0.74	0.99	[0.93, 1.06]	0.88	1.01	[0.96, 1.05]	0.84	0.99	[0.94, 1.04]

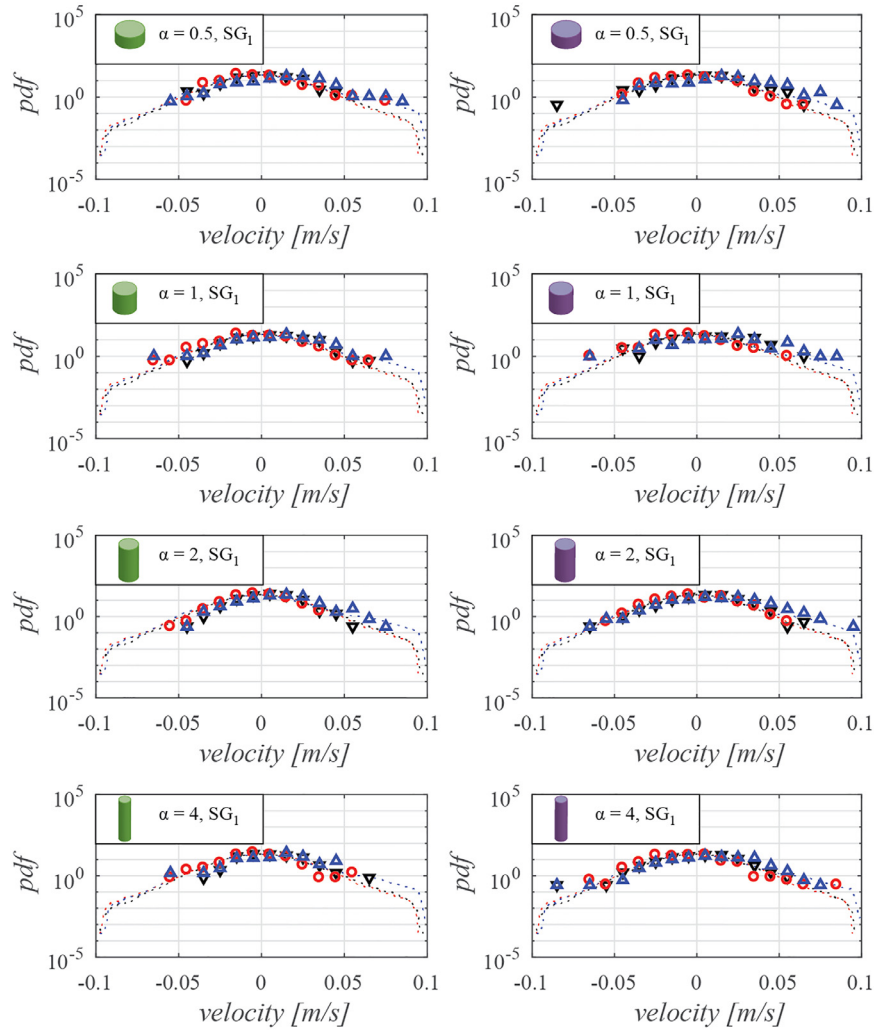


Fig. A.1. Probability density functions of the single-phase (unladen) fluid velocity (dotted lines), overlaid with a normalized histogram of observed cylinder velocities. Here, black lines/markers represent the x-component u , red lines/markers represent the y-component v , and blue lines/markers represent the z-component w . Markers used to denote cylinder velocity histogram are point-down triangles (u), circles (v), and point-up triangles (w). Data are separated by aspect ratio and specific gravity. (For interpretation of the references to colour in this figure legend, the reader is referred to the web version of this article.)

plotted in Fig. 3, showing that the confidence interval for the best-fit slope includes 1 for virtually all cases. Table A.3 shows the fit parameters for a piecewise representation of the same data (divided by quartile), showing that \mathbf{u}_f and \mathbf{u}_p are less well-correlated

in the center of the observed data range than at the extremes of \mathbf{u}_f . Fig. A.1 shows the pdfs (by component) of the unladen fluid velocities together with a normalized histogram of the cylinder velocities, separated by aspect ratio and specific gravity.

Table A.3

Correlation coefficients of cylinder velocity \mathbf{u}_p regressed to surrounding fluid velocity \mathbf{u}_f , separated by dimensional velocity component (u , v , and w) and cylinder type (aspect ratio α and specific gravity SG. Data are further separated by quartile of $|\mathbf{u}_f|$: each pair of values \mathbf{u}_p and \mathbf{u}_f , representing an independent measurement, is sorted by the magnitude of \mathbf{u}_f and separated into quartiles. We then calculate Pearson's correlation coefficient for each quartile separately, in a piecewise fashion. For almost all cylinder types, across all three dimensions, the first and fourth quartile of data are more closely correlated than the second and third quartiles, indicating that at the extremes of \mathbf{u}_f , the cylinder velocity \mathbf{u}_p is more closely correlated with the fluid velocity than it is in the middle of the data range.

		$\rho(u_p, u_f)$					$\rho(v_p, v_f)$				$\rho(w_p, w_f)$			
	α	N	Q1	Q2	Q3	Q4	Q1	Q2	Q3	Q4	Q1	Q2	Q3	Q4
SG ₁	0.5	185	0.76	0.38	0.23	0.75	0.71	0.51	0.55	0.89	0.88	0.60	0.56	0.84
	1	192	0.72	0.53	0.38	0.71	0.94	0.41	0.47	0.91	0.89	0.55	0.25	0.83
	2	412	0.59	0.26	0.27	0.65	0.82	0.43	0.60	0.78	0.53	0.96	0.50	0.83
	4	133	0.65	0.28	0.69	0.81	0.90	0.75	0.55	0.94	0.67	0.99	0.52	0.83
SG ₂	0.5	303	0.73	0.33	0.47	0.78	0.86	0.53	0.64	0.76	0.87	0.66	0.41	0.80
	1	101	0.72	0.33	0.63	0.72	0.88	0.61	0.47	0.84	0.85	0.87	0.40	0.88
	2	413	0.75	0.35	0.23	0.57	0.82	0.46	0.41	0.80	0.84	0.52	0.49	0.68
	4	369	0.52	0.51	0.37	0.63	0.80	0.46	0.43	0.83	0.67	0.57	0.58	0.62

Supplementary material

Supplementary material associated with this article can be found, in the online version, at doi:[10.1016/j.ijmultiphaseflow.2019.103120](https://doi.org/10.1016/j.ijmultiphaseflow.2019.103120).

References

- Angle, B.R., Rau, M.J., Byron, M., 2019. Effect of mass distribution on falling cylindrical particles at intermediate reynolds numbers. ASME 2019 Fluids Engineering Division Summer Meeting. American Society of Mechanical Engineers.
- Ardekani, M.N., Costa, P., Breugem, W.P., Brandt, L., 2016. Numerical study of the sedimentation of spheroidal particles. *Int. J. Multiph. Flow* 87, 16–34.
- Armenio, V., Fiorotto, V., 2001. The importance of the forces acting on particles in turbulent flows. *Phys. Fluids* 13 (8), 2437–2440.
- Bagchi, P., Balachandar, S., 2002. Shear versus vortex-induced lift force on a rigid sphere at moderate Re. *J. Fluid Mech.* 473, 379–388.
- Bagchi, P., Balachandar, S., 2002. Steady planar straining flow past a rigid sphere at moderate Reynolds number. *J. Fluid Mech.* 466, 365–407.
- Bagchi, P., Balachandar, S., 2003. Effect of turbulence on the drag and lift of a particle. *Phys. Fluids* (1994–present) 15 (11), 3496–3513. doi:[10.1063/1.1616031](https://doi.org/10.1063/1.1616031).
- Bagchi, P., Balachandar, S., 2003. Inertial and viscous forces on a rigid sphere in straining flows at moderate Reynolds numbers. *J. Fluid Mech.* 481, 105–148.
- Bagheri, G., Bonadonna, C., 2016. On the drag of freely falling non-spherical particles. *Powd. Technol.* 301, 526–544.
- Bellani, G., Byron, M.L., Collignon, A.G., Meyer, C.R., Variano, E.A., 2012. Shape effects on turbulent modulation by large nearly neutrally buoyant particles. *J. Fluid Mech.* 712, 41–60.
- Bellani, G., Nole, M.A., Variano, E.A., 2013. Turbulence modulation by large ellipsoidal particles: concentration effects. *Acta Mechanica* 224 (10), 2291–2299.
- Bellani, G., Variano, E.A., 2012. Slip velocity of large neutrally buoyant particles in turbulent flows. *New J. Phys.* 14 (12), 125009. doi:[10.1088/1367-2630/14/12/125009](https://doi.org/10.1088/1367-2630/14/12/125009).
- Bellani, G., Variano, E.A., 2014. Homogeneity and isotropy in a laboratory turbulent flow. *Exp. Fluids* 55 (1), 1646–1657.
- Birouk, M., Sarh, B., Gökalp, I., 2003. An attempt to realize experimental isotropic turbulence at low Reynolds number. *Flow Turbul. Combust.* 70 (1–4), 325–348.
- Bridgeman, J., Jefferson, B., Parsons, S.A., 2009. Computational fluid dynamics modelling of flocculation in water treatment: a review. *Engineering Applications of Computational Fluid Mechanics* 3 (2), 220–241.
- Brush, L.M., Ho, H.W., Singamsetti, S.R., 1962. A study of sediment in suspension. *Bulletin of the International Association of Scientific Hydrology* 59, 293–310.
- Byron, M., Einarsson, J., Gustavsson, K., Voth, G., Mehlig, B., Variano, E., 2015. Shape-dependence of particle rotation in isotropic turbulence. *Phys. Fluids* 27 (3), 035101.
- Byron, M.L., Variano, E.A., 2013. Refractive-index-matched hydrogel materials for measuring flow-structure interactions. *Exp. Fluids* 54 (2), 1456–1461.
- Calzavarini, E., Volk, R., Lévy, E., Pinton, J.F., Toschi, F., 2012. Impact of trailing wake drag on the statistical properties and dynamics of finite-sized particle in turbulence. *Physica D: Nonlinear Phenomena* 241 (3), 237–244. doi:[10.1016/j.physd.2011.06.004](https://doi.org/10.1016/j.physd.2011.06.004).
- Christiansen, E.B., Barker, D.H., 1965. The effect of shape and density on the free settling of particles at high Reynolds numbers. *Am. Inst. Chem. Eng. J.* 11 (1), 145–151. doi:[10.1002/aic.690110130](https://doi.org/10.1002/aic.690110130).
- Cisse, M., Homann, H., Bec, J., 2013. Slipping motion of large neutrally buoyant particles in turbulence. *J. Fluid Mech.* 735. doi:[10.1017/jfm.2013.490](https://doi.org/10.1017/jfm.2013.490).
- Csanady, G.T., 1963. Turbulent diffusion of heavy particles in the atmosphere. *J. Atmos. Sci.* 20 (3), 201–208. doi:[10.1175/1520-0469\(1963\)020<0201:TDOHPI>2.0.CO;2](https://doi.org/10.1175/1520-0469(1963)020<0201:TDOHPI>2.0.CO;2).
- Darwin, C., 1953. Note on hydrodynamics. *Math. Proc. Cambridge Philos. Soc.* 49 (2), 342–354.
- De Jong, J., Cao, L., Woodward, S., Salazar, J., Collins, L., Meng, H., 2009. Dissipation rate estimation from pIV in zero-mean isotropic turbulence. *Exp. Fluids* 46 (3), 499–515.
- Dietrich, W.E., 1982. Settling velocity of natural particles. *Water Resour. Res.* 18 (6), 1615–1626. doi:[10.1029/WR018i06p01615](https://doi.org/10.1029/WR018i06p01615).
- Do-Quang, M., Amberg, G., Brethouwer, G., Johansson, A.V., 2014. Simulation of finite-size fibers in turbulent channel flows. *Phys. Rev. E* 89 (1), 013006.
- Elghobashi, S., 1994. On predicting particle-laden turbulent flows. *Appl. Scientific Res.* 52 (4), 309–329.
- Esteban, L.B., Shrimpton, J., Ganapathisubramani, B., 2018. Edge effects on the fluttering characteristics of freely falling planar particles. *Phys. Rev. Fluids* 3 (6), 064302.
- Esteban, L.B., Shrimpton, J., Ganapathisubramani, B., 2019. Three dimensional wakes of freely falling planar polygons. *Exp. Fluids* 60 (7), 114.
- Ferrante, A., Elghobashi, S., 2003. On the physical mechanisms of two-way coupling in particle-laden isotropic turbulence. *Phys. Fluids* 15 (2), 315–329.
- Field, W.G., 1968. Effects of density ratio on sedimentary similitude. *J. Hydraulics Div.* 94 (3), 705–720.
- Fornari, W., Picano, F., Brandt, L., 2016. Sedimentation of finite-size spheres in quiescent and turbulent environments. *J. Fluid Mech.* 788, 640–669.
- Fornari, W., Picano, F., Sardina, G., Brandt, L., 2016. Reduced particle settling speed in turbulence. *J. Fluid Mech.* 808, 153–167.
- Fuchs, H.L., Gerbi, G.P., 2016. Seascape-level variation in turbulence-and wave-generated hydrodynamic signals experienced by plankton. *Prog. Oceanogr.* 141, 109–129.
- Good, G.H., Ireland, P.J., Bewley, G.P., Bodenschatz, E., Collins, L.R., Warhaft, Z., 2014. Settling regimes of inertial particles in isotropic turbulence. *J. Fluid Mech.* 759. doi:[10.1017/jfm.2014.602](https://doi.org/10.1017/jfm.2014.602).
- Hölzer, A., Sommerfeld, M., 2008. New simple correlation formula for the drag coefficient of non-spherical particles. *Powd. Technol.* 184 (3), 361–365.
- Hwang, W., Eaton, J., 2004. Creating homogeneous and isotropic turbulence without a mean flow. *Exp. Fluids* 36 (3), 444–454.
- Jiménez, J., 1997. Oceanic turbulence at millimeter scales. *Scientia Marina* 61, 47–56.
- Katija, K., Dabiri, J.O., 2009. A viscosity-enhanced mechanism for biogenic ocean mixing. *Nature* 460 (7255), 624.
- Kjørboe, T., Andersen, K., Dam, H., 1990. Coagulation efficiency and aggregate formation in marine phytoplankton. *Marine Biol.* 107 (2), 235–245.
- Krawczynski, J., Renou, B., Danaila, L., 2010. The structure of the velocity field in a confined flow driven by an array of opposed jets. *Phys. Fluids* 22 (4), 045104.
- Kulick, J.D., Fessler, J.R., Eaton, J.K., 1994. Particle response and turbulence modification in fully developed channel flow. *J. Fluid Mech.* 277, 109–134.
- Lopez, D., Guazzelli, E., 2017. Inertial effects on fibers settling in a vortical flow. *Phys. Rev. Fluids* 2 (2), 024306.
- Loth, E., 2008. Drag of non-spherical solid particles of regular and irregular shape. *Powd. Technol.* 182 (3), 342–353.
- Lundell, F., Söderberg, L.D., Alfredsson, P.H., 2011. Fluid mechanics of papermaking. *Annu. Rev. Fluid Mech.* 43, 195–217.
- Makita, H., Sassa, K., 1991. Active turbulence generation in a laboratory wind tunnel. In: *Advances in Turbulence 3*. Springer, pp. 497–505.
- Mandø, M., Rosendahl, L., 2010. On the motion of non-spherical particles at high Reynolds number. *Powd. Technol.* 202 (1–3), 1–13. doi:[10.1016/j.powtec.2010.05.001](https://doi.org/10.1016/j.powtec.2010.05.001).
- Marchioli, C., Fantoni, M., Soldati, A., 2010. Orientation, distribution, and deposition of elongated, inertial fibers in turbulent channel flow. *Phys. Fluids* 22 (3), 033301.
- Maxey, M., 1987. The gravitational settling of aerosol particles in homogeneous turbulence and random flow fields. *J. Fluid Mech.* 174, 441–465.
- Maxey, M., Corrsin, S., 1986. Gravitational settling of aerosol particles in randomly oriented cellular flow fields. *J. Atmos. Sci.* 43 (11), 1112–1134.
- Maxey, M.R., 1990. On the advection of spherical and non-spherical particles in a non-uniform flow. *Philos. Trans. R. Soc. Lond. A* 333 (1631), 289–307. doi:[10.1098/rsta.1990.0162](https://doi.org/10.1098/rsta.1990.0162).
- Meek, C.C., Jones, B.G., 1973. Studies of the behavior of heavy particles in a turbulent fluid flow. *J. Atmos. Sci.* 30 (2), 239–244.
- Murray, S.P., 1970. Settling velocities and vertical diffusion of particles in turbulent water. *J. Geophys. Res.* 75 (9), 1693–6.
- Nielsen, P., 2007. Mean and Variance of the Velocity of Solid Particles in Turbulence. In: *Particle-Laden Flow*. Springer, pp. 385–391.
- Parsa, S., Calzavarini, E., Toschi, F., Voth, G.A., 2012. Rotation rate of rods in turbulent fluid flow. *Phys. Rev. Lett.* 109 (13), 134501.
- Pope, S.B., 2001. *Turbulent flows*. IOP Publishing.
- Reeks, M., McKee, S., 1984. The dispersive effects of basset history forces on particle motion in a turbulent flow. *Phys. Fluids* 27 (7), 1573–1582.
- Schmeeckle, M.W., Nelson, J.M., Pitlick, J., Bennett, J.P., 2001. Interparticle collision of natural sediment grains in water. *Water Resour. Res.* 37 (9), 2377–2391.
- Shin, H., Maxey, M., 1997. Chaotic motion of nonspherical particles settling in a cellular flow field. *Phys. Rev. E* 56 (5), 5431.
- Tooby, P.F., Wick, G.L., Isaacs, J.D., 1977. The motion of a small sphere in a rotating velocity field: a possible mechanism for suspending particles in turbulence. *J. Geophys. Res.* 82 (15), 2096–2100. doi:[10.1029/JC082i015p02096](https://doi.org/10.1029/JC082i015p02096).
- Variano, E.A., Cowen, E.A., 2008. A random-jet-stirred turbulence tank. *J. Fluid Mech.* 604, 1–32.
- Villermaux, E., Sixou, B., Gagne, Y., 1995. Intense vortical structures in grid-generated turbulence. *Phys. Fluids* 7 (8), 2008–2013.
- Voth, G.A., Soldati, A., 2017. Anisotropic particles in turbulence. *Annu. Rev. Fluid Mech.* 49, 249–276.
- Wang, L.P., Maxey, M.R., 1993. Settling velocity and concentration distribution of heavy particles in homogeneous isotropic turbulence. *J. Fluid Mech.* 256, 27–68. doi:[10.1017/S0022112093002708](https://doi.org/10.1017/S0022112093002708).
- Webster, D.R., Brathwaite, A., Yen, J., 2004. A novel laboratory apparatus for simulating isotropic oceanic turbulence at low Reynolds number. *Limnol. Oceanogr.: Methods* 2 (1), 1–12.
- Yin, C., Rosendahl, L., Kær, S.K., Sørensen, H., 2003. Modelling the motion of cylindrical particles in a nonuniform flow. *Chem. Eng. Sci.* 58 (15), 3489–3498.
- Yudine, M.I., 1959. Physical Considerations on Heavy-Particle Diffusion. In: *Landsberg, H.E., Van Mieghem, J. (Eds.), Advances in Geophysics*, 6. Elsevier, pp. 185–191.
- Zhang, H., Ahmadi, G., Fan, F.-G., McLaughlin, J., 2001. Ellipsoidal particles transport and deposition in turbulent channel flows. *Int. J. Multiph. Flow* 27 (6), 971–1009.
- Zhao, F., van Wachem, B.G.M., 2013. Direct numerical simulation of ellipsoidal particles in turbulent channel flow. *Acta Mechanica* 224 (10), 2331–2358. doi:[10.1007/s00707-013-0921-3](https://doi.org/10.1007/s00707-013-0921-3).
- Zhao, L., Marchioli, C., Andersson, H.I., 2014. Slip velocity of rigid fibers in turbulent channel flow. *Phys. Fluids* 26 (6), 063302. doi:[10.1063/1.4881942](https://doi.org/10.1063/1.4881942).